J. Fluid Mech. (1985), *vol.* 156, *pp.* 439–461
Printed in Great Britain

Vortices incident upon a leading edge: instantaneous pressure fields

By RUHI KAYKAYOGLU AND DONALD ROCKWELL
Department of Mechanical Engineering and Mechanics, Lehigh University, Bethlehem, Pennsylvania 18015

(Received 15 August 1984)

A mixing-layer flow formed by merging of high- and low-speed streams leads to successive generation of vortices of the same sense that impinge upon a leading edge. Distortion of each incident vortex, secondary-vortex shedding, and 'sweeping' of flow about the tip of the edge are related to the instantaneous pressure fields via simultaneous flow visualization and pressure measurement. The instantaneous pressure fields are interpreted as downstream travelling waves along the upper and lower surfaces of the edge; in turn, these wavelike pressure variations are linked to the visualized vortex patterns adjacent to each surface.

Near the tip of the edge, where rapid flow distortion occurs, the pressure fields are non-wavelike; on the lower surface of the tip, negligible streamwise phase variations of fluctuating pressure are associated with secondary shedding there, while on the upper surface there is a phase jump. This jump can be as large as π when the incident vortex impinges directly upon, or passes just below, the tip of the edge. Downstream of this near-tip region, the wavelike pressure fields show short and long wavelengths on the lower and upper surfaces respectively. These wavelengths, in turn, differ substantially from the wavelength of the incident-vortex instability.

Irrespective of the transverse location of the incident vortex with respect to the leading edge, maximum pressure amplitude always occurs at the tip of the edge; it takes on its largest value when the scale of secondary shedding from the tip of the edge is most pronounced. Moreover, the fact that the net force on the edge scales with tip-pressure amplitude underscores the crucial role of the local flow distortions in the tip region.

1. Introduction

Impingement of vortical structures on leading edges occurs with varying degrees of coherence in a variety of flows such as vortex impingement upon wings, helicopter and turbomachinery blades, corners of cavities, and downstream cylinders. Such interactions are central to determining the unsteady edge loading and associated noise generation. If the incident vortical structure is 'compact' and the lengthscale of the edge also satisfies conditions of compactness, then one can deduce directly the nature of the far-field sound from knowledge of the unsteady hydrodynamic field at the edge (Crighton 1975). Of course, the magnitude of the resultant edge force follows from the amplitude and phasing of the unsteady (distributed) pressure field at the edge; it, in turn, is tied to local flow distortions in the leading-edge region.

Most investigations have focused on theoretical simulation of these unsteady-shear-flow–body interactions, as discussed in recent reviews of Rockwell (1983) and Goldstein (1984). However, little is known of the detailed mechanics of such

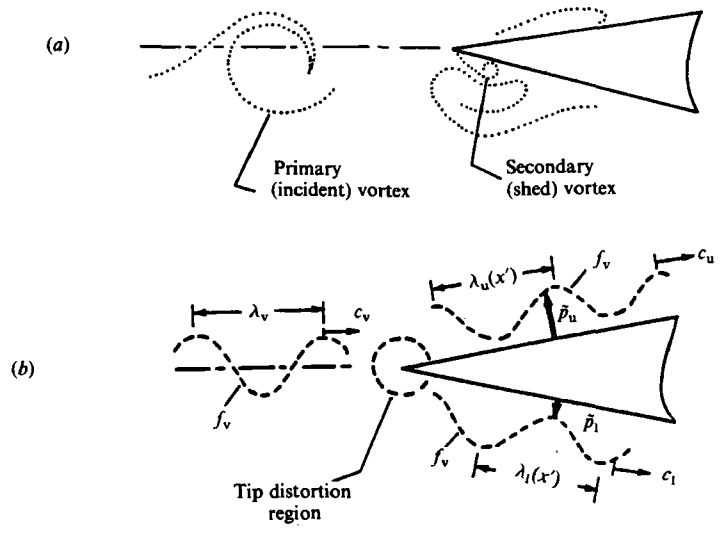

FIGURE 1. Simplified schematic showing characteristics of incident vortex wave, and upper and lower surface pressure waves at the leading edge.

interactions, for which nonlinear and viscous effects may prove to be important. Recently, Ziada & Rockwell (1982) (hereinafter referred to as Z–R) defined the basic mechanisms of vortex–edge interaction for the case of a periodic train of vortices incident upon a wedge and related them to the overall force on the wedge surface. From their studies, it is evident that the amplitude of the induced force is a strong function of the type of interaction mechanism at the edge, characterized by distortion of the incident vortex and secondary vortex shedding from the tip of the edge. Z–R define details of the vortex–edge interaction such as the angle of the separation line and the position of the shed vortex as functions of the interaction mechanism, both of which are related to the phase angle of the induced force relative to the position of the incident vortex.

To date, however, there has been no investigation of the instantaneous pressure field on the surface of the edge and its relation to the mechanism of vortex–edge interaction. Clearly, if one is to design properly leading edges/impingement surfaces and control the character of the incident vortical structures that minimize the vortex-induced force at the edge, it is essential to know the detailed amplitude and phase characteristics of the fluctuating pressure field in the edge region, and their relation to the principal types of vortex–edge interaction.

When the incident vortices interact with the edge, resultant vortex-like structures travel downstream along the upper and lower surfaces of the edge, inducing pressure fluctuations along each surface (figure 1); it is helpful to interpret the unsteady surface pressures $\tilde{p}_u$ and $\tilde{p}_l$ in terms of downstream travelling waves (λ_u, c_u; λ_l, c_l), and link them to the characteristics of the incident vortex wave (λ_v, c_v). The objectives of this investigation are to determine the pressure amplitude and phase variations associated with this wavelike representation, and their relation to the vortex-edge distortion mechanisms.

2. Experimental system and instrumentation

2.1. *Means of generation of incident vortex*

Figure 2 shows the central features of the experimental test section, involving generation of a mixing-layer flow from the trailing edge of a plate; details are given in Z–R. Here we focus on some essential details. The unstable mixing layer evolved into a well-defined vortex, which subsequently impinged upon the wedge. During the course of the experiment, the impingement edge was moved in the transverse direction, allowing study of various interaction mechanisms. As demonstrated by Z–R, the structure of the incident vortex remained essentially unaltered, irrespective of the relative location of the edge within the range examined herein. The free-stream-velocity ratio of the high- to low-speed side was $U_1/U_2 = 2.85 \pm 0.05$, with respective momentum thicknesses $\theta_{01} = 0.62$ mm and $\theta_{02} = 0.68$ mm, θ_0 representing their sum. The corresponding Reynolds number was $R_{\theta_0} = 157$, or $R_{\theta_R} = 230$ (see page 81 of Z–R 1982). Here θ_R is defined as the local momentum thickness at the station $11\theta_R$ upstream of the leading edge of the wedge. The length of the wedge was $l' = 36.5\theta_R$; in order to avoid undesirable effects of coherent vortex shedding from the downstream part of the wedge, a long plate ($l = 240\theta_R$) was attached to it; moreover, a vortex-shedding attenuator was mounted on the downstream edge of the plate. Other dimensions of the system were: $b'/\theta_0 \equiv$ thickness of trailing of plate $= 3$; T'/θ_0 thickness of impingement wedge $= 15$; and $L/\theta_0 \equiv$ length from trailing edge to tip of impingement wedge $= 89$.

2.2. *Character of incident vortex*

In Z–R, the structure of the incident vortex (figure 3*a*) is discussed in detail; by simulating it with the nonlinear inviscid model of Stuart (1967), it is possible to determine its degree of concentration of vorticity. Here we point out some of the essential features of the mean- and fluctuating-velocity distributions. As shown in figure 3(*b*), the mean-velocity profile $\overline{u}(y)$ generated from the trailing edge of figure 2 is well predicted by the Stuart model; it is approximated by a $\tanh(y)$ distribution. Moreover, the distribution of fluctuation velocity at the vortex frequency $\tilde{u}_{\rm rms}(\beta)$, where β is dimensionless f, also agrees well with the theory of Stuart if one employs a vorticity-concentration parameter $\alpha = 0.7$.

The data points shown in figures 3(*b*) and (*c*) represent three different values of vortex–edge offset (see Z–R) underscoring the fact that the structure of the incident vortex is invariant with transverse offset of the impingement wedge. Further, figure 3(*d*) shows the distribution of dimensionless $\tilde{v}_{\rm rms}(\beta)$; if one considers it together with the $\tilde{u}_{\rm rms}(\beta)$ distribution of figure 3(*c*), it is evident that there are strong gradients in the magnitudes of $\tilde{u}$ and $\tilde{v}$ near the centre of the vortex. Consequently, we expect large changes in the leading-edge pressure field for small offset of the vortex centre relative to the tip of the leading edge; indeed, as will be demonstrated below, offsets of the order of the local momentum thickness θ_R can effect substantial modification of the amplitude and phase distributions of the unsteady field.

2.3. *Flow visualization*

Flow visualization involved both hydrogen-bubble and dye-injection techniques. In the case of dye injection, the dye emanated from the upper surface of the trailing edge of the plate. As demonstrated in Z–R, the vortex patterns have the same form as those visualized by the hydrogen-bubble technique involving timeline markers generated well upstream of the leading edge. A constant-source, 1000 W light was

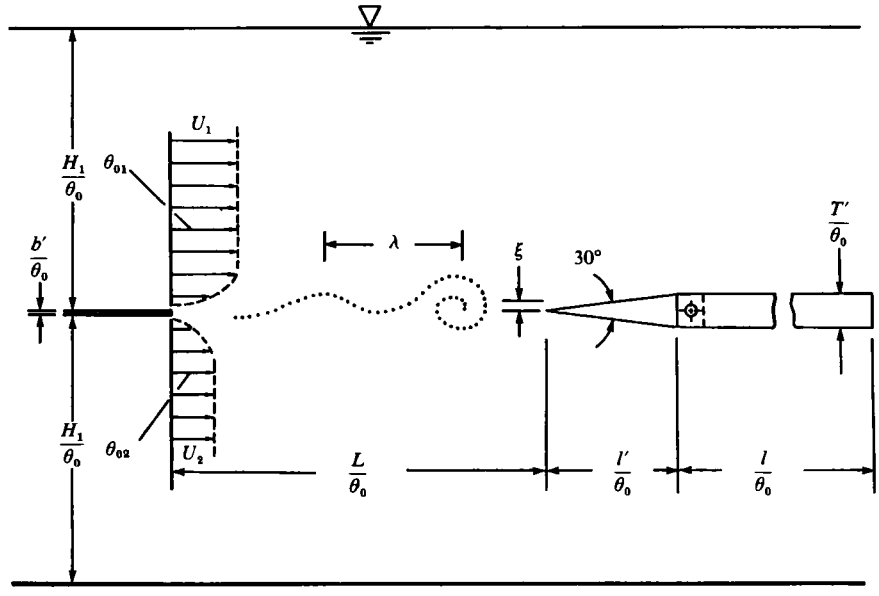

FIGURE 2. Schematic of experimental test section showing means of incident vortex generation from trailing edge of splitter plate and location of leading edge of wedge.

located behind the test section; by placing translucent plastic between the light source and the plane of visualization, it was possible to achieve diffuse illumination without concentrated glare. For the hydrogen-bubble technique, different arrangements of platinum wires located adjacent to, and in some cases passing through, the tip of the edge provided insight into the interaction process near the tip beyond that attained by Z–R. In these cases, lighting was provided by two 90 W stroboscopic lamps located on either side of the test section and aimed at the tip of the edge.

This visualization allowed direct correlation of the instantaneous pressure field on the edge with visualized vortex–edge interaction by recording the vortex patterns and instantaneous traces of the pressure transducer outputs simultaneously on an Instar IV high-speed video system having a split-screen capability. This Instar television system has vertical and horizontal sweep frequencies of 120 Hz and 25.2 kHz, a resolution of 250 lines, and a framing rate of 120 frames/s.

2.4. *Measurement of unsteady pressure fields*

The unsteady pressure field was measured using high-sensitivity Kulite pressure transducers with a paralene coating (model XCS-190-2D). A total of nine pressure taps were located at the leading edge ($x' = 0$ in figure 6) and along the upper and lower surfaces downstream of the leading edge at $x' = 0.16$, 0.48, 0.96, and 1.90 cm. These tap locations correspond, respectively, to dimensionless x' normalized with respect to incident wavelength of the vortical structures λ of $x'/\lambda = 0.04$, 0.125, 0.25, and 0.50. Owing to the small angle of the wedge (30° shown in figure 2), it was necessary to stagger the locations of the pressure taps in the spanwise direction. Successive taps were located distances of $z/\lambda = 0$, 0.70, 0.98, 1.25 and 1.52, where z is distance from the midplane of the wedge and λ is again the wavelength between incident vortices. Extensive flow visualization using hydrogen-bubble and dye-injection techniques showed that the flow was two-dimensional in the spanwise direction over this domain of measurement.

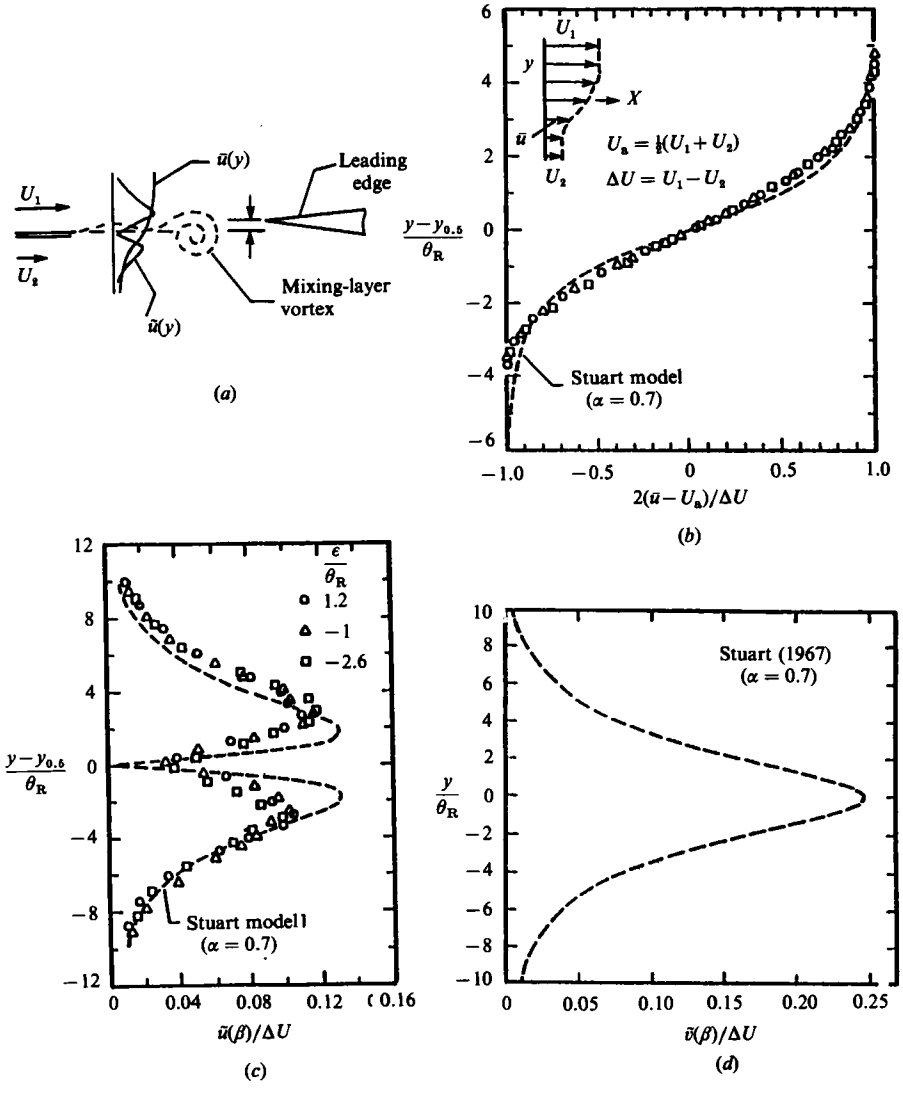

FIGURE 3. Mean- and fluctuation-velocity distributions of incident vortex. (After Ziada & Rockwell 1982.)

The diameter of each pressure tap was 0.8 mm, except the leading-edge tap which had a diameter of 0.4 mm. Channels connecting the taps to the transducers had diameters ranging from 0.4 to 3.1 mm and lengths from 5.2 to 10.1 cm. A prime concern was possible amplitude and phase distortion due to the distance from the tap to the sensing surface of the transducer. However, since the frequency was low (of the order of 1 Hz) and water was employed as the working fluid, extensive frequency response tests showed amplitude and phase distortions to be negligible for the experimental conditions investigated herein. The natural frequencies of the pressure tap–channel combinations were in the range 41–60 Hz, giving, at worst, amplitude distortion of 0.1 % and phase distortion of 0.2°. In making pressure measurements, it was necessary to employ only two transducers, one measuring the pressure tap of interest, the other serving as a reference signal. By employing a small valve in each pressure line at a

location downstream from the wedge, it was possible to successively correlate signals between the reference and active taps. In doing so, cross-spectral analysis using a MINC minicomputer provided the amplitude and relative phase of the pressure at the tap under consideration. The sampling rate was 50 Hz, corresponding to 25 oscillation cycles per sample. A total rate of six cross-spectra were averaged to give the final value of amplitude and phase at each pressure-measurement station. Since the flow was essentially periodic, it is possible to construct the instantaneous pressure fields from the respective amplitudes and phases of these surface pressures.

3. Interaction mechanisms at the leading edge

The mechanism of interaction at the leading edge depends strongly upon the relative offset between the incident vortex and the tip of the edge. Figure 4 shows cases where the major share of the vortex passes well below, slightly above, and well above the leading edge in the photos of the top, middle, and bottom *rows* respectively. In the first two *columns* of photos, the hydrogen-bubble wire that liberates pulsed timelines is located well upstream of the edge, providing a view of the evolved vortex formation/interaction in the vicinity of the leading edge; on the other hand, in the third column of photos, the wire is located at the leading edge, thereby highlighting the process of secondary vortex shedding.

In the first column of photos, taken at instant B at which the vertical force on the edge is maximum negative, it is evident that secondary-vortex shedding from the underside of the edge is about to occur. For the second column of photos E, the instantaneous force is maximum positive; note the pronounced formation of a secondary vortex when the incident vortex is slightly above the edge (middle photo). The third column of photos, with the wire located at the leading edge, shows secondary shedding; it takes the form of bubble concentrations of varying scale on the underside of the edge, depending on the relative offset of the incident vortex. These photos evidence continued rolling up of the incident vortex downstream of the edge (top and bottom photos), or dominance of secondary-vortex shedding from the edge (middle photo).

If one views these flow patterns on the upper and lower surfaces of the edge in conjunction with the wavelike representation of figure 1, it follows that the amplitude and phase variation of the pressure field along the surface of the edge will, in turn, be a function of the basic types of interaction mechanisms shown in figure 4. In general, we must expect that the speed with which these wavelike disturbances move downstream will be different for the upper and lower surfaces of the edge. That this is so is suggested by the series of photos shown in figure 5(*a*), corresponding to the case of strong secondary-vortex shedding depicted in the middle row of photos of figure 4. By successively tracking the second to fifth photos in figure 5(*a*), it is evident that the crest of bubbles on the upper surface (designated in the schematic) moves downstream considerably faster than that corresponding to the shed vortex along the bottom surface. The instantaneous pressure-field measurements described subsequently corroborate this observation.

Further features of the tip interaction region are brought forth in figure 5(*b*) which, for the same conditions as figure 5(*a*), shows streaklines of the distorted incident vortex along the upper surface, associated sweeping of flow about the tip, and formation of the secondary vortex. The instantaneous streamline curvature of this flow about the tip gives large-amplitude pressure fluctuations there, as evidenced by measurements of this investigation.

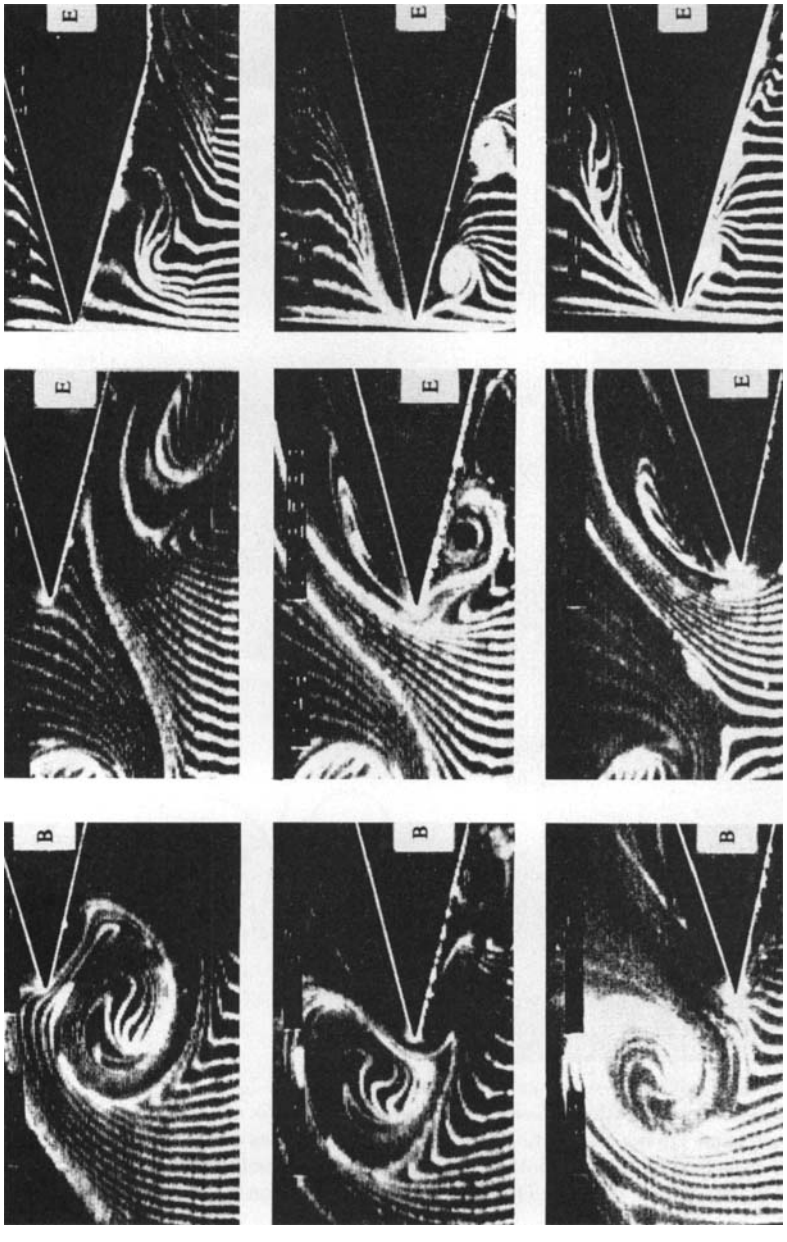

FIGURE 4. Overview of vortex–edge interaction mechanisms for cases where incident vortex is well below, slightly above, and well above leading edge shown, respectively, in top, middle, and bottom rows. (Photos from Ziada & Rockwell 1982.)

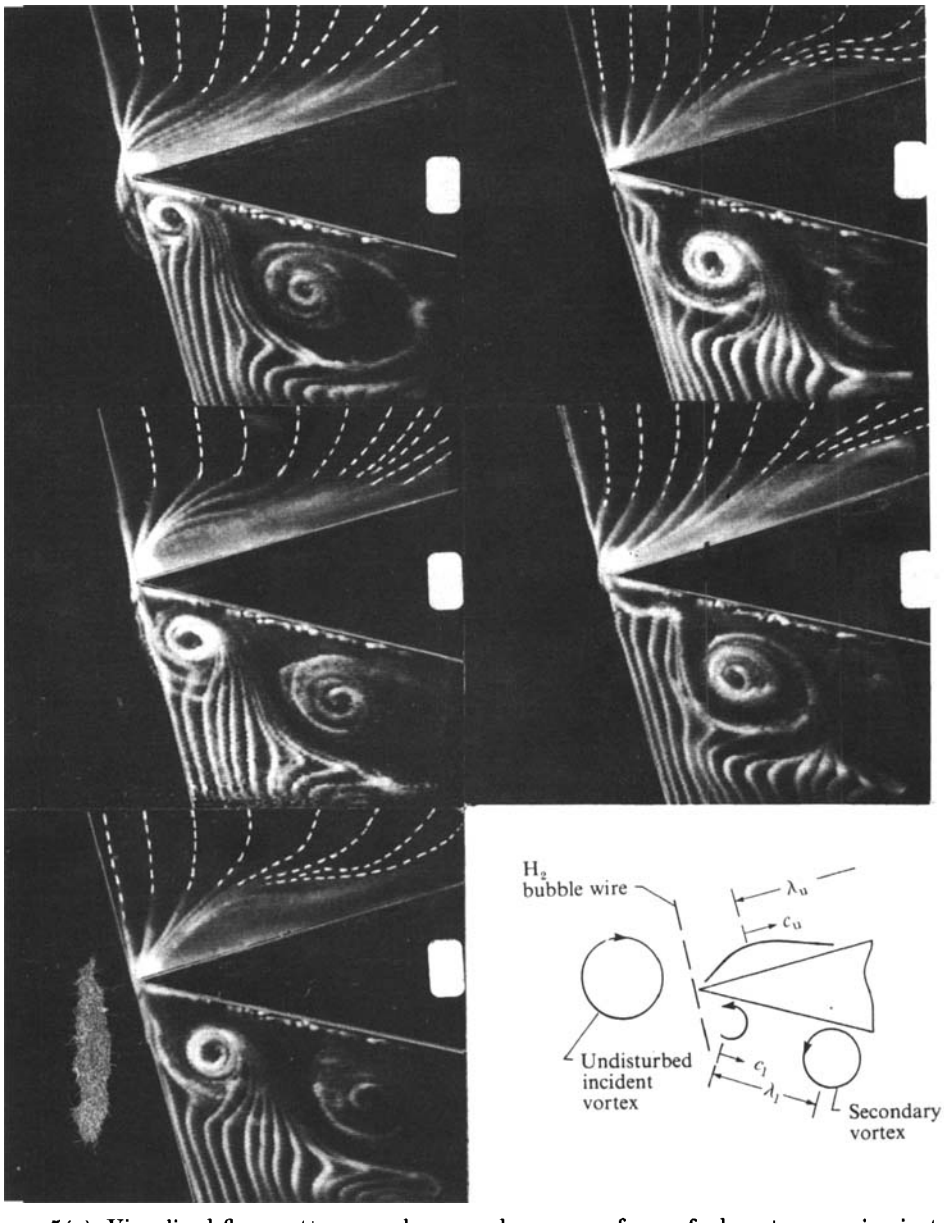

FIGURE 5(*a*). Visualized flow patterns on lower and upper surfaces of edge at successive instants of time showing differences in propagation speed of the wavelike motions of the distorted incident vortex and the secondary shed vortex along the upper and lower surfaces of the edge respectively. Wire is located at tip of edge and inclined in both xy and yz planes producing crossing of timelines, most evident in secondary vortex of photo *b*. (Dashed lines are drawn on shadowed timelines.)

On the basis of the foregoing flow visualization of figure 5, we can already provide a qualitative basis for interpreting the streamwise phase $\phi(x')$ measurements herein. If we take the following equations,

$$c_{u,l} = f\lambda_{u,l} = 2\pi f \Big/ \left[\frac{d\phi_{u,l}}{dx}\right],$$

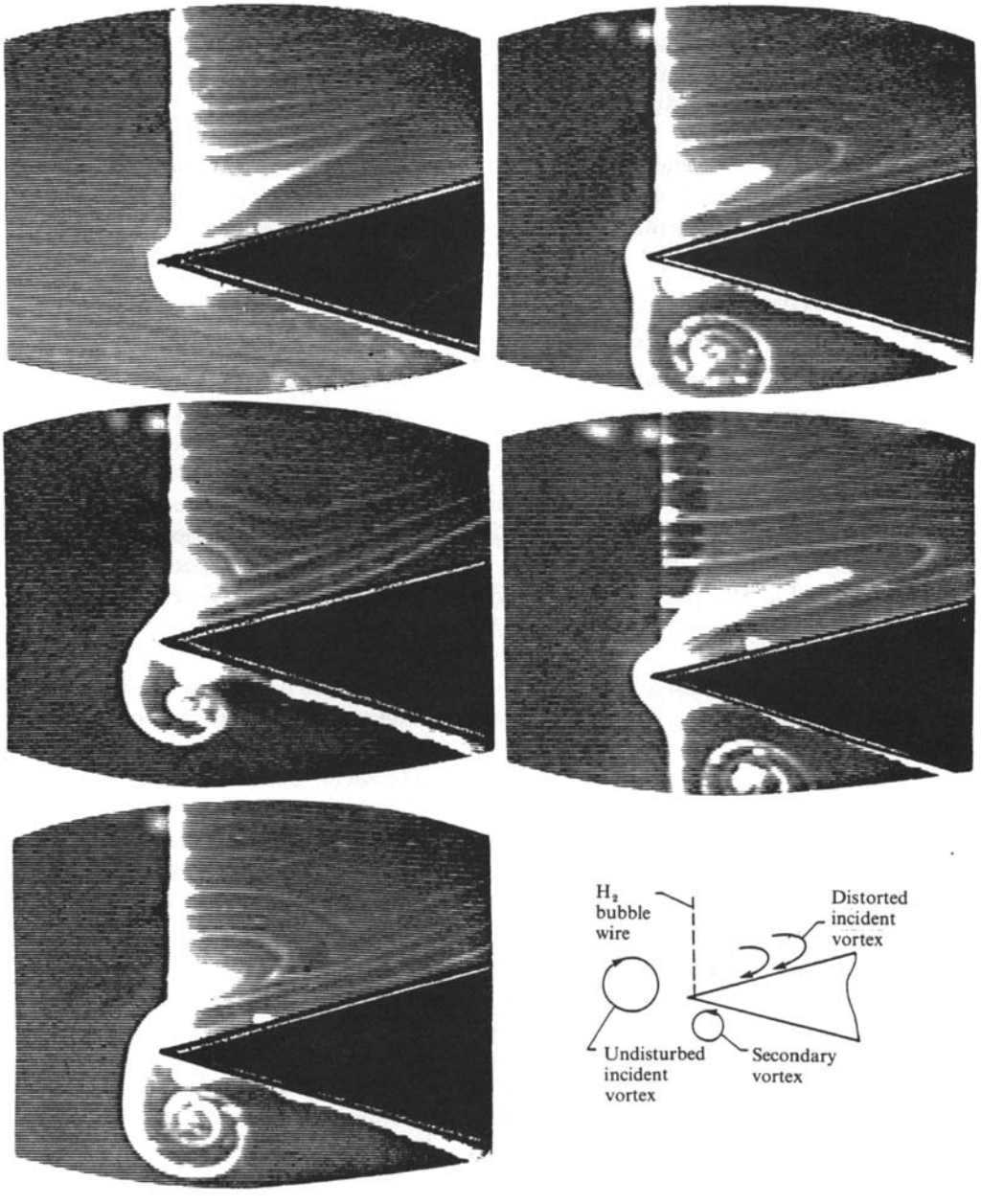

FIGURE 5(*b*). Visualized flow patterns near tip of edge showing streaklines of distorted incident vortex, and sweeping of flow about tip leading to formation of secondary vortex. Vertical bubble wire passes through the edge at a location 0.3λ downstream of the tip.

to give the relation between phase ϕ, propagation speed c, wavelength λ, and frequency f, then the relatively high propagation speed on the upper surface of figure 5*a* corresponds to a long wavelength λ, or a mild phase variation $\mathrm{d}\phi/\mathrm{d}x'$, in comparison with those values along the bottom surface. Consequently, the pressure fluctuations along the upper surface will tend to produce a large amplitude force there since the pressure fluctuations tend to act in phase. The converse reasoning holds for the lower surface where the phase speed of the wavelike motion is considerably

smaller. Of course, one must know the corresponding pressure-amplitude distribution $\tilde{p}$ in order to determine the actual force values on the upper and lower surfaces. Moreover, we expect ϕ, λ, and c, as well as the amplitude of the pressure fluctuations $\tilde{p}$, to be strong functions of streamwise distance x', especially near the tip of the edge; one cannot deduce such features from the foregoing visualization alone.

In the following, we focus on quantitative interpretation of the detailed pressure loading (amplitude $\tilde{p}(x')$ and phase $\phi_{\tilde{p}}(x')$) along the surfaces of the edge, in conjunction with the type of interaction mechanisms at the edge.

4. Pressure fields

4.1. *Amplitude and phase variations in leading-edge region*

Amplitude and phase distributions of the fluctuating pressure field along the upper and lower surfaces of the edge follow from application of the cross-spectral analysis described in §2. Figure 6 shows resultant variations of pressure amplitude $\tilde{p}$ and phase ϕ. The normalizing pressure $\tilde{p}_{\max}$ corresponds to the maximum pressure at the tip of the leading edge (i.e. $x' = 0$); it occurs at $\xi/\theta_R = -2.0$. In all cases the phase at the tip $[\phi_{\tilde{p}}]$ is set equal to zero, thereby serving as the phase reference for the upper and lower surfaces. Also shown in each case is a representative photo taken at time $t/T = \frac{4}{5}$, where T is the period of the oscillation cycle, and $t = 0$ corresponds to the instant at which the vortex centre is a distance 0.3λ upstream of the tip of the leading edge.

Concerning the variation of pressure amplitude along the upper and lower surfaces, it is evident from figure 6 that, for all vortex–edge interaction mechanisms, the maximum occurs at the tip of the edge, $x' = 0$; the pressure amplitude decreases in the region immediately downstream of the tip. However, the pressure amplitude at the tip takes on quite different values depending upon the degree of severing of the incident vortex, and associated secondary shedding from the tip. Minimum amplitude occurs when the major share of the vortex is swept above or below the edge, while maximum amplitude occurs when it is severed in such a fashion that the scale of the shed vortex is maximum.

Important in interpreting the maximum pressure amplitude at the tip is the sweeping of fluid about the edge from the upper to lower surface demonstrated in the series of photos of figure 5; these photos correspond to the pronounced secondary shedding at $\xi/\theta_R = -2$ in figure 6. Evidently, the pressure gradients associated with the instantaneous streamline curvature there are particularly large. This effect appears to be present in varying degrees for all interaction mechanisms addressed herein, i.e. for all values of ξ/θ_R in figure 6.

Regarding the phase variations corresponding to the foregoing amplitude variations, figure 6 shows that along the lower side of the edge, in the early region of interaction ($x'/\lambda \gtrsim 0.1$), the phase gradient $\mathrm{d}\phi_{\tilde{p}l}/\mathrm{d}x'$ is very small or even negative. This initial region corresponds to the onset of secondary-vortex shedding which occurs, with varying scale, for all interaction mechanisms. Clearly, in this domain of the leading edge, where rapid distortions of the flow are occurring, one cannot speak of a wavelike representation of the unsteady pressure field. However, at larger values of x'/λ, the phase variations have substantial slopes; using the relation $c = 2\pi f/[\mathrm{d}\phi/\mathrm{d}x']$, one can deduce the phase speed c_l of the corresponding pressure wave motion, relative to that of the incident vortices c_v, $0.3 \leqslant c_l/c_v \leqslant 0.8$ (see figure 1 for notation). On the upper surface of the edge, all interaction mechanisms show a rapid adjustment of phase, corresponding to a sudden increase, or even jump, near the tip of the leading edge. Physically it is associated with the aforementioned 'sweeping' about the edge. The

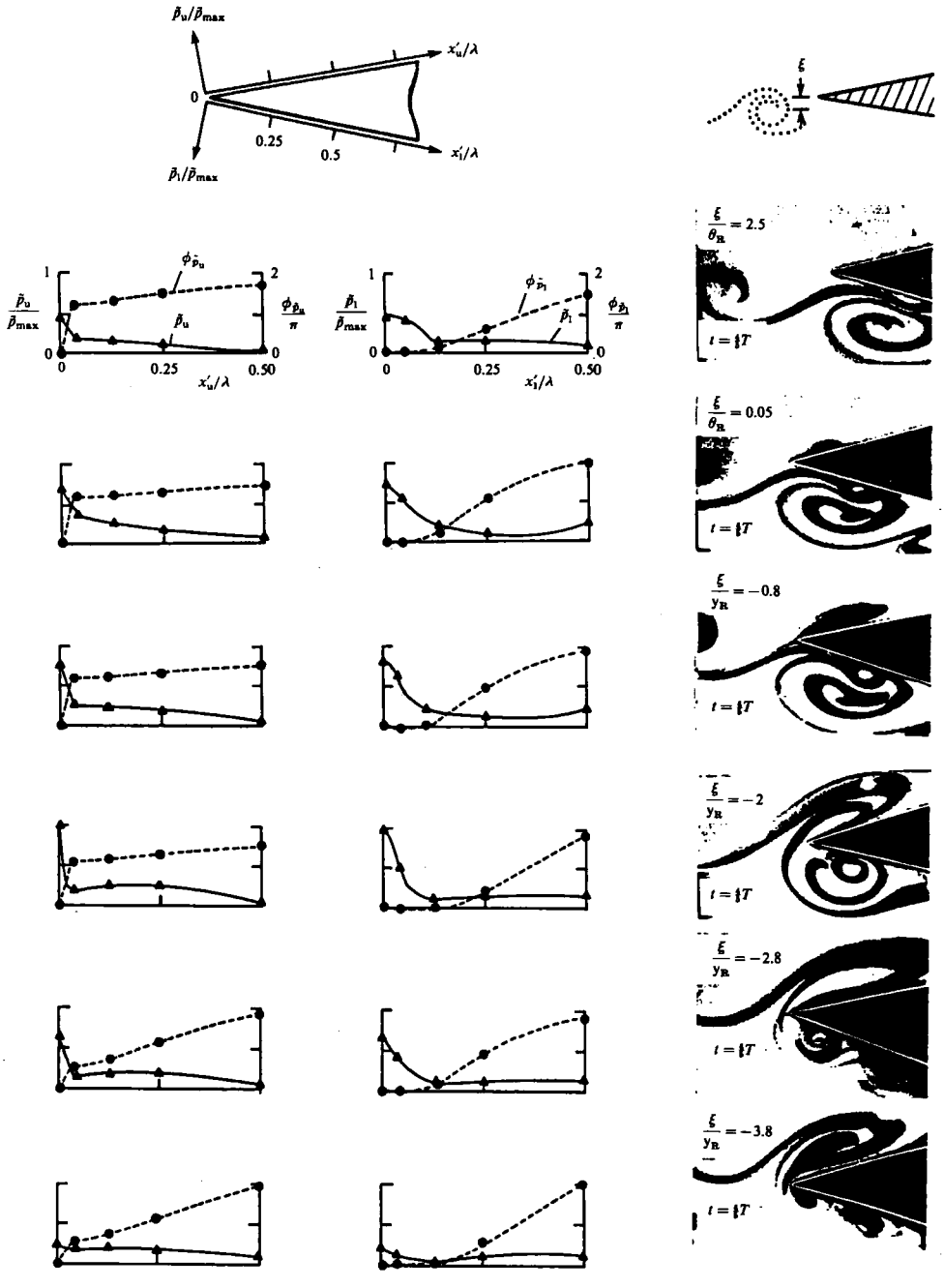

FIGURE 6. Amplitude and phase variations of fluctuating pressure field on upper and lower surfaces of leading edge.

streamwise phase gradients $d\phi_{\tilde{p}_u}/dx'$ are very mild, indicating a large value of wavelength λ_u and phase speed c_u, except in those cases where a major share of the incident vortex is swept above the edge ($\xi/\theta_R = -2.8, -3.8$); for these interactions, $d\phi_{\tilde{p}_u}/dx'$ becomes larger, substantially reducing the values of λ_u and c_u. We note that these observations on variation of phase speeds c_l, and c_u downstream of the tip region are also in accord with what one expects due to partitioning of the incident mean

shear layer (figure 3) at the edge. As the edge is moved downward into lower-speed regions of the incident flow, corresponding to increasingly negative ξ/θ_R in figure 6, there is a tendency for $d\phi/dx'$ to increase (at large x'/λ) corresponding to a decrease in phase speed; this trend is especially evident along the upper surface of the edge.

In summary, one may make the following observations concerning the unsteady loading, corresponding to the integrated pressures on the surface of the edge. Close to the tip on the lower surface, the very mild phase variations provide a strongly correlated pressure field and high loading; in contrast, at locations very close to the tip of the upper surface, the drastic variation in phase provides considerably weaker loading in this near region. However, downstream of this tip region, the situation is reversed, in that phase variations along the lower surface are substantial, while those along the upper surface are very mild. Consequently, there will be relatively weak and strong loading respectively in these regions.

4.2. *Instantaneous pressure fields*

With the amplitude and phase variations of the fluctuating pressure field of figure 6 at hand, it is possible to construct the instantaneous pressure fields on the upper and lower surfaces of the edge at successive instants of time t, where $t = 0$ corresponds to the location of the incident vortex centre a distance 0.3λ upstream of the edge; this definition holds for all interaction mechanisms.In each composite showing pressure fields and corresponding visualization (figures 7*a–f*), the instantaneous distributions on the upper x'_u and lower x'_l surfaces of the edge and the interaction mechanism at that instant are given at five values of time t over the oscillation cycle T. For all interactions, we see that the maximum negative pressure occurs at initiation of secondary-vortex shedding from the tip of the edge; it occurs in the range $\frac{1}{5} \lesssim t/T \lesssim \frac{2}{5}$ for all interaction mechanisms. With regard to the instantaneous pressure variations on the lower surface of the edge, the maximum negative pressure there follows the centre of the vortex shedding from the tip, giving rise to a wavelike motion of the pressure field on that surface. The wavelength of this pressure wave along the lower surface is a function of x', i.e. $\lambda_l = \lambda_l(x')$. However, if one considers an average wavelength $\bar{\lambda}_l$ along the lower surface, its value is much smaller than that of the incident vortices of wavelength λ, i.e. $\bar{\lambda}_l \simeq \frac{1}{2}\lambda$.

Corresponding pressure distributions along the upper surface in figure 7 reflect the mild streamwise phase variations of figure 6, and represent large values of wavelength λ_u. On the other hand, for cases $\xi/\theta_R = -2.8$ and -3.8 in figure 7, where the incident vortex remains relatively intact as it negotiates the edge region, the phase variations are substantially larger, giving rise to smaller values of wavelength λ_u.

5. Forces on the leading edge

In order to determine the degree to which the pressure field in the vicinity of the tip of the edge influences the force on the wedge as a whole, one may integrate the instantaneous pressure field, properly accounting for streamwise phase variations, over various distances from the leading edge, i.e. $\lambda/K = \frac{1}{12}, \frac{1}{6}, \frac{1}{3}$, and $\frac{1}{2}$, as shown schematically in figure 8. One may write the equations for the forces on the upper and lower surfaces, F'_u and F'_l, as well as the net force F'_{net} as:

$$F'_{u,l} = \int_0^{1/K} P'_{u,l}\left(\frac{x'}{\lambda}, \frac{t}{T}\right) d\left(\frac{x'}{\lambda}\right);$$

$$F'_{net} = F'_u + F'_l.$$

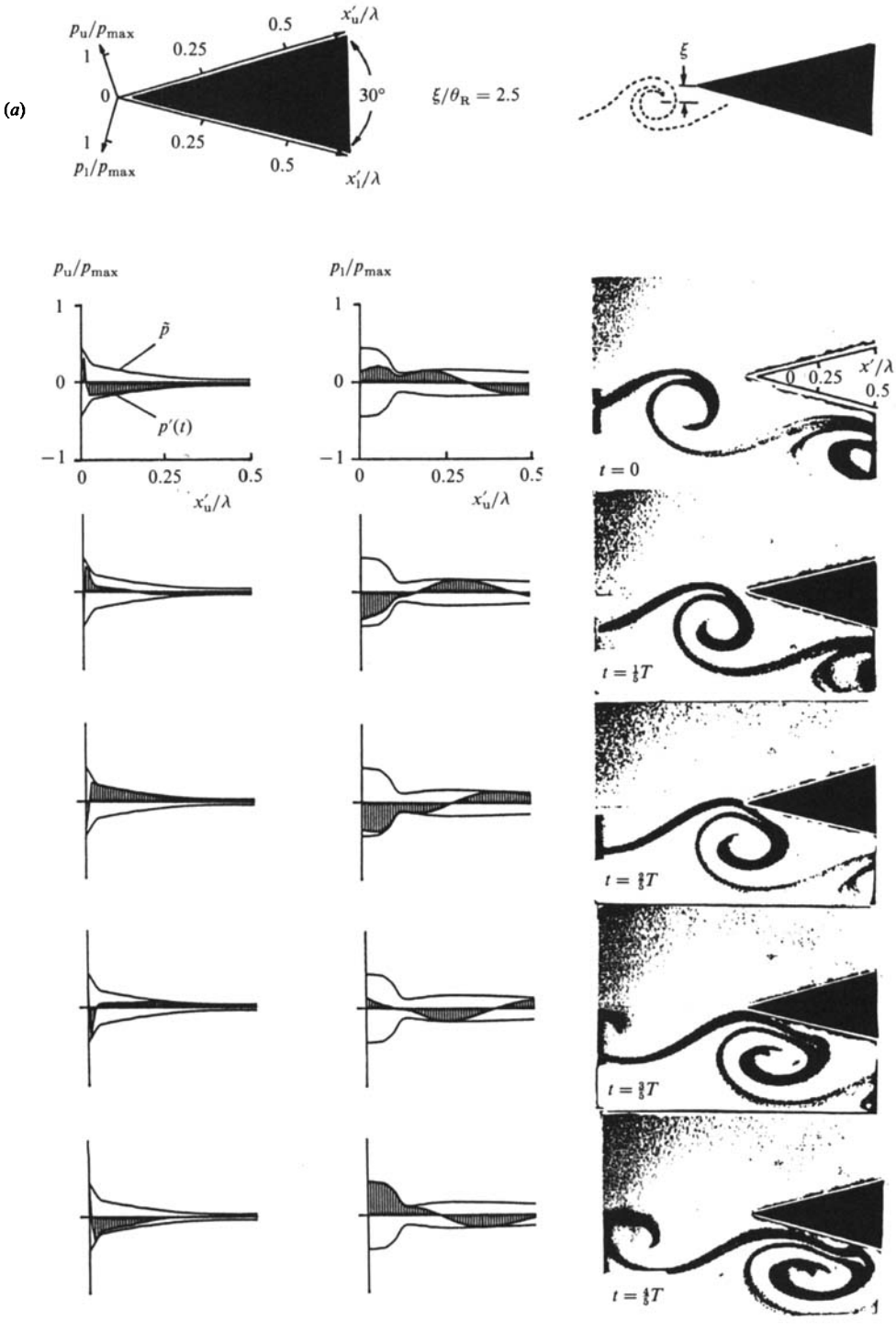

FIGURE 7 (*a*). For caption see p. 456.

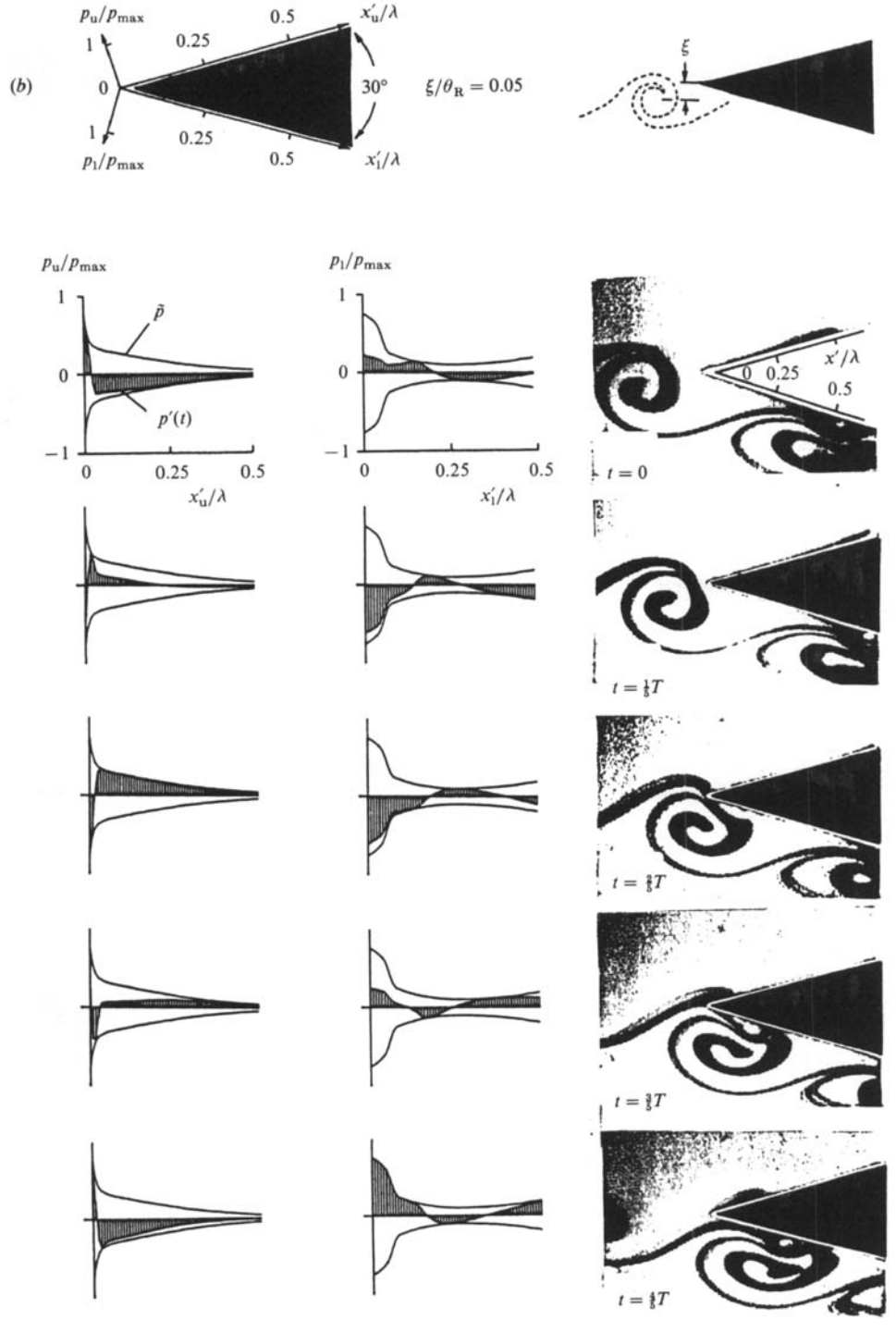

FIGURE 7 (*b*). For caption see p. 456.

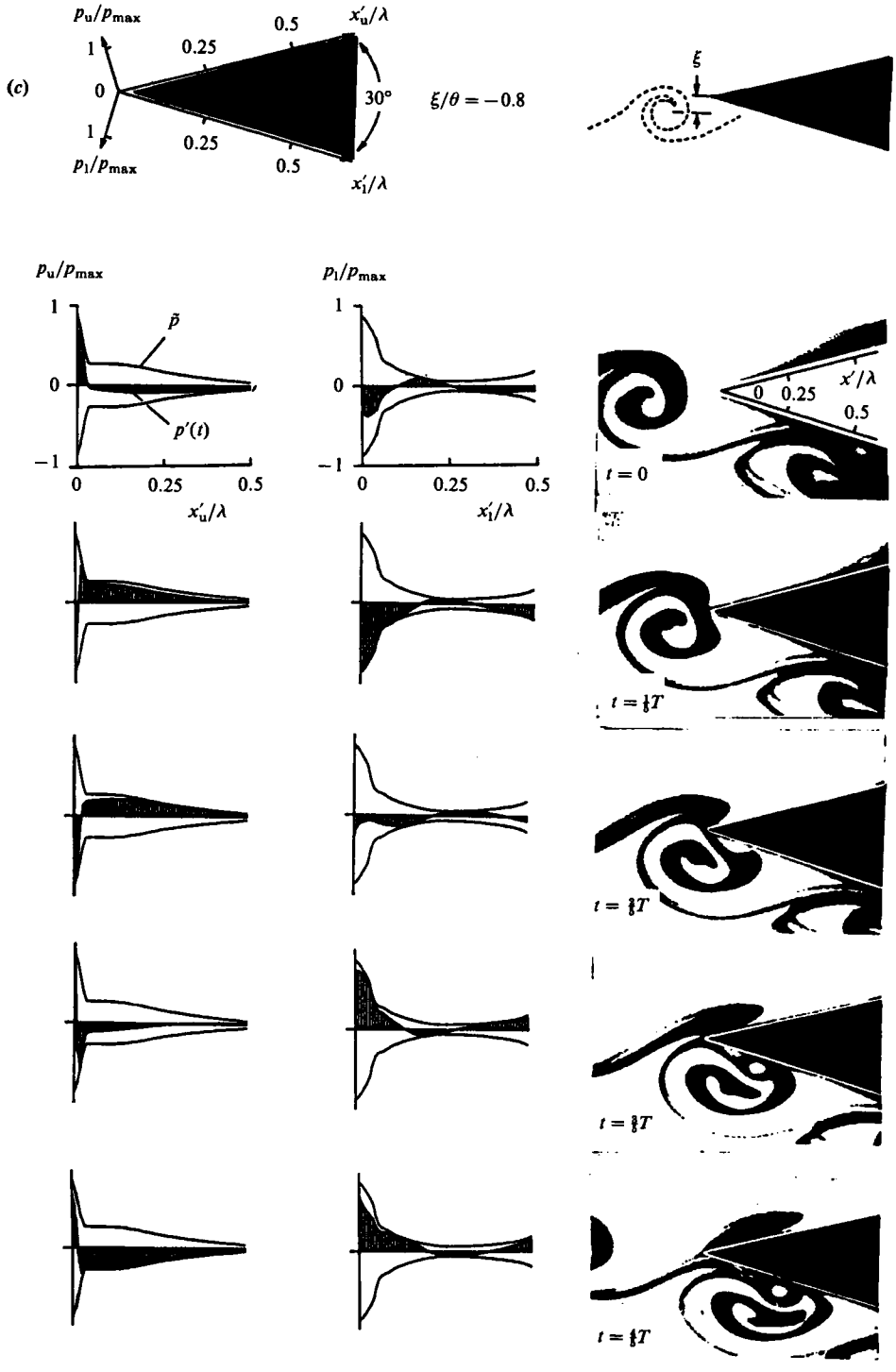

FIGURE 7 (*c*). For caption see p. 456.

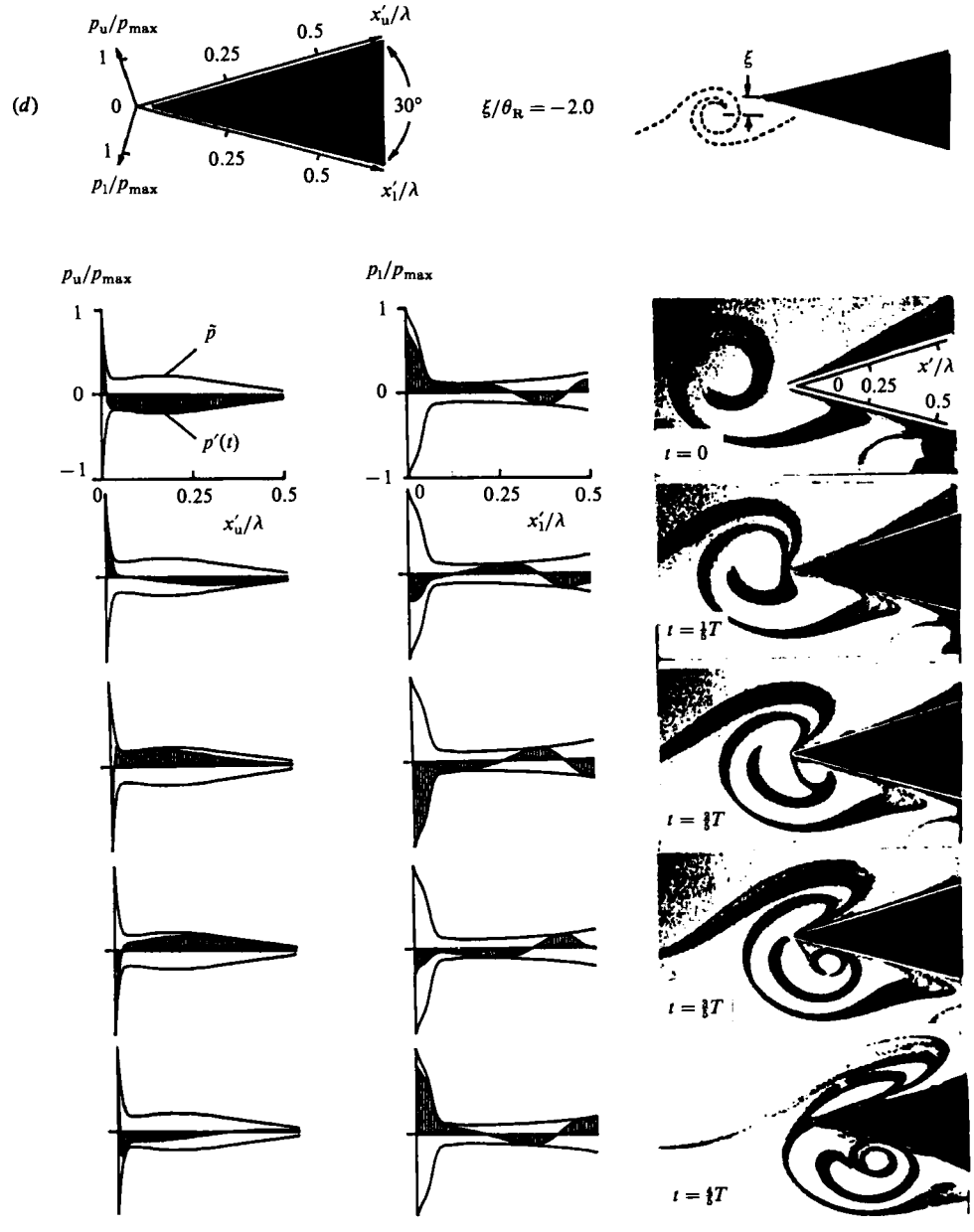

FIGURE 7 (*d*). For caption see p. 456.

Figure 9 shows the resultant forces F'_u, F'_l, and F'_{net}; all are normalized with respect to the same force F'_{max}, which is the maximum force amplitude obtained over the range of interaction mechanisms examined; it occurs at $\xi/\theta_R = -0.8$. In these force plots, the reference time $t = 0$ is the same as that in the photos of figure 7. Moreover, the symbols plotted are not data points; they simply identify the curves corresponding to different domains of integration.

In cases where there is vortex formation of substantial scale on the underside of the edge ($0.05 \leqslant \xi/\lambda_R \leqslant -2.8$), the phase and amplitude of the force on the lower surface

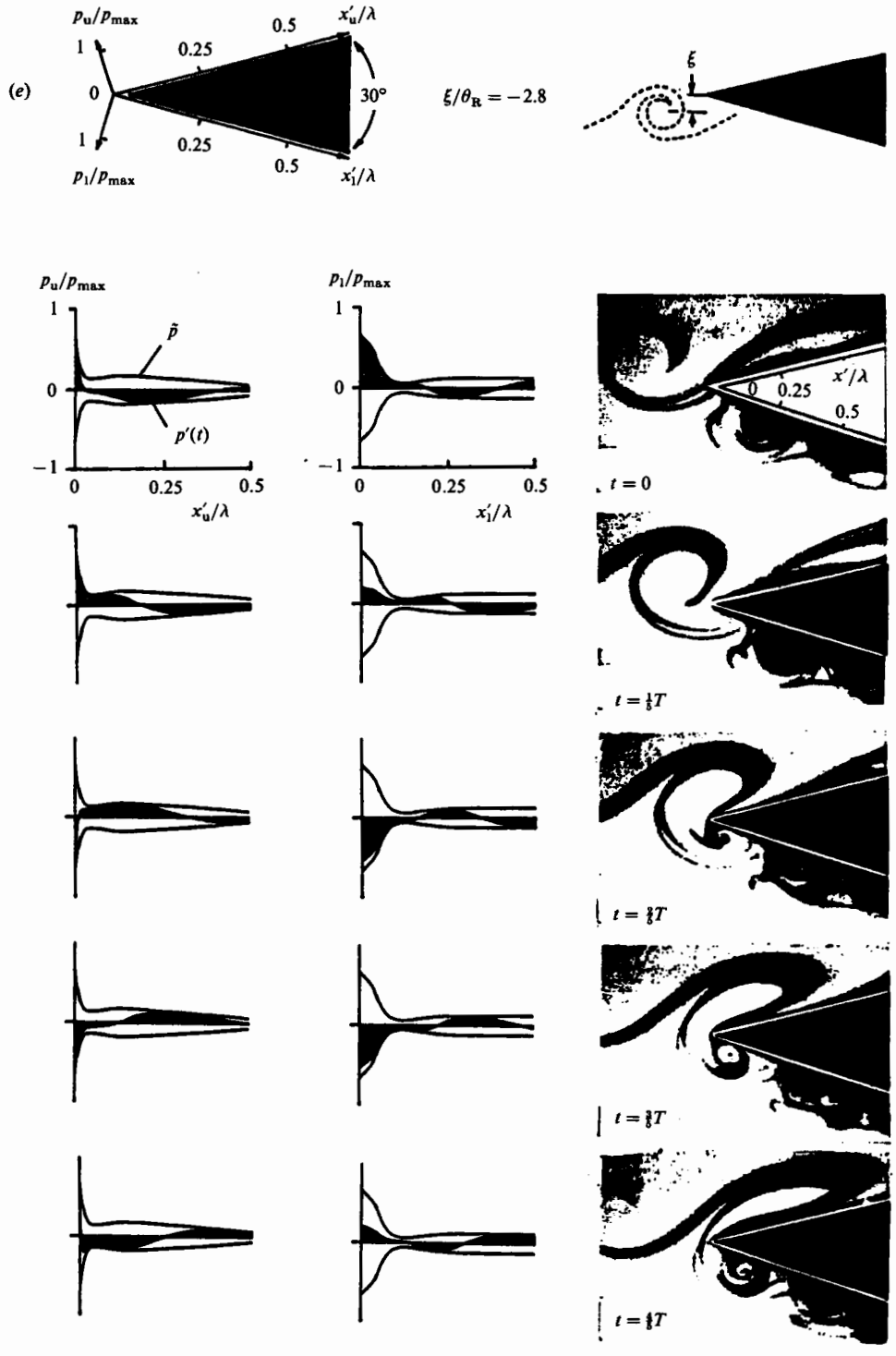

FIGURE 7 (*e*). For caption see p. 456.

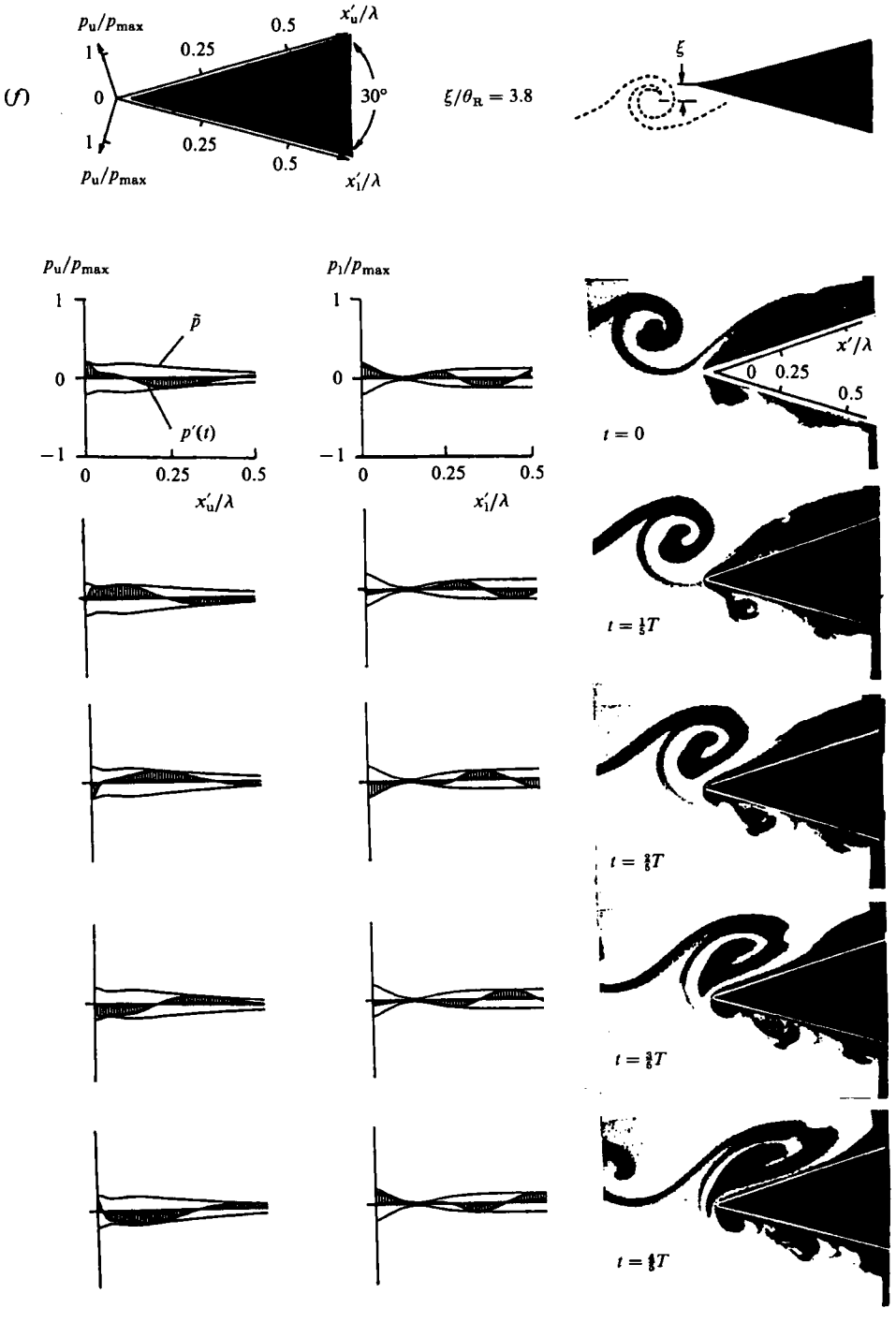

FIGURE 7. Instantaneous pressure fields and corresponding vortex–edge interaction mechanisms for various locations of vortex relative to leading edge. $L/\theta_R = 42$, $Re_{\theta_R} = 230$.

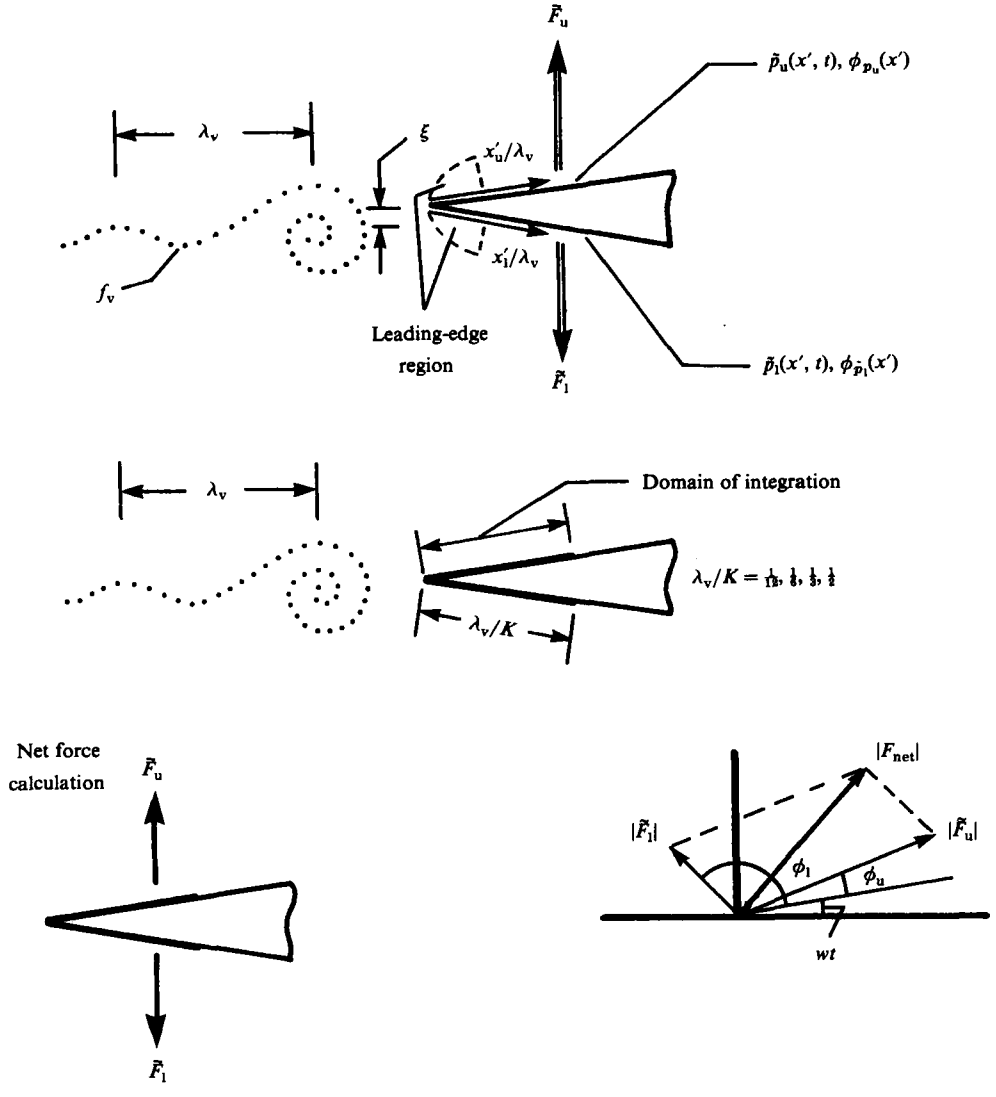

FIGURE 8. Schematic showing varying domains of integration of pressure fields from tip of leading edge onward, $F'_u(t/T) = \int_0^{1/K} p'_u(x'/\lambda_v, t/T)\,\mathrm{d}(x'/\lambda_v)$, $F'_l(t/T) = \ldots$, and relation between upper ($\bar{F}_u$), lower ($\bar{F}_l$), and ($\bar{F}_{net}$) forces.

are only weakly dependent on the domain of integration. Physically, this means that almost the entire loading on the lower surface of the edge occurs within a distance of $\frac{1}{12}\lambda$ from the tip of the leading edge.

In contrast, the corresponding forces on the upper surface show strong variations in amplitude and phase as the domain of integration is varied; this occurs for all interaction mechanisms, and is due to the mild streamwise phase gradient along the upper surface (see figures 6 and 7).

The net force F'_{net} acting on the edge is obtained by adding the upper and lower surface forces F'_u and F'_l, properly accounting for the phase angle between them. The maximum value of F'_{net} occurs at $\xi/\theta_R = -0.8$, not at $\xi/\theta_R = -2.0$ where the shed vortex has its largest scale and the leading-edge pressure is maximum; this effect

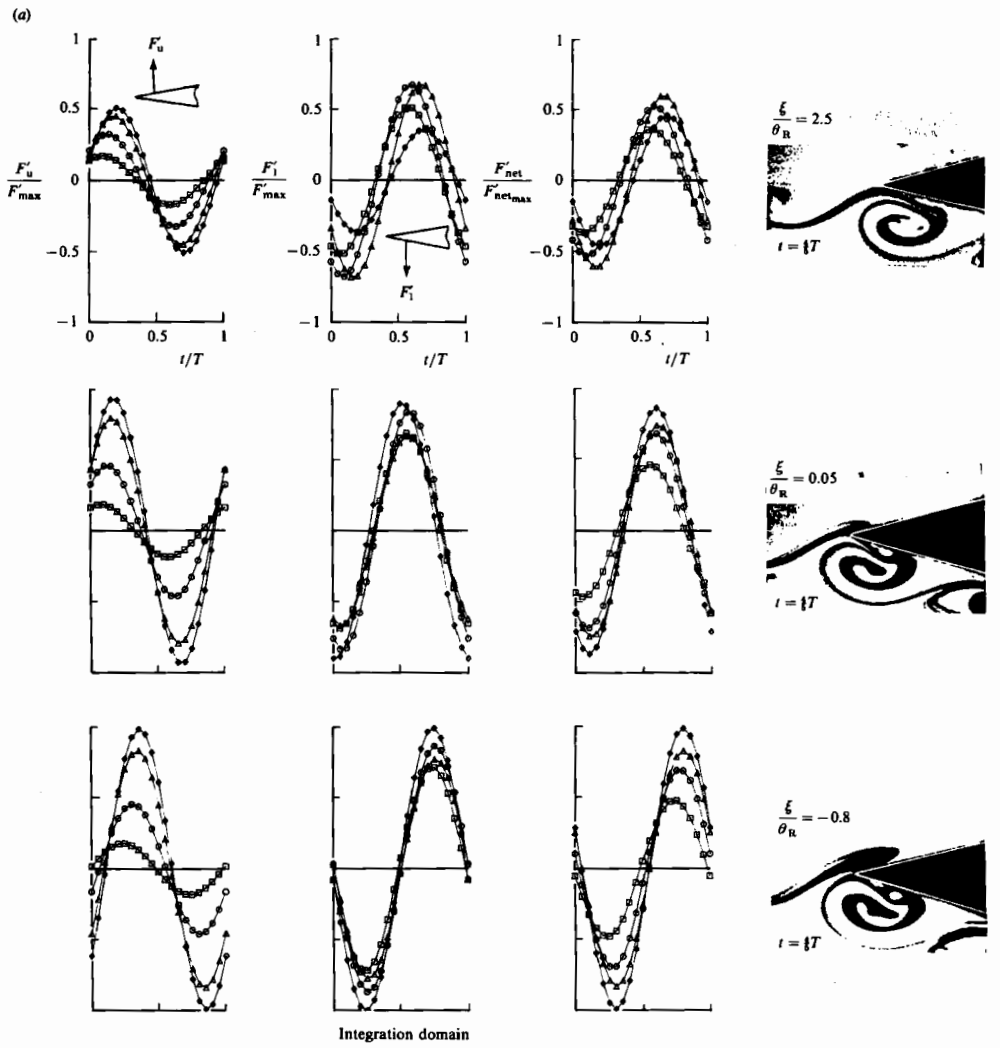

FIGURE 9 (*a*). For caption see opposite.

is primarily due to the fact that the pressure amplitudes immediately downstream of the tip of the edge decay more rapidly in the former, as compared to the latter, case.

6. Overview of forces on the edge and the pressure at the tip of the leading-edge

Figure 10 gives a direct comparison between the net force on the edge measured with a strain-gauge arrangement $\tilde{F}_{Z-R}$ (see Z − R), the forces calculated from instantaneous pressure fields integrated over the surfaces of the edge $\tilde{F}_{net}$ as described in the foregoing, and the variation of leading-edge pressure $[\tilde{P}]_{x'=0}$ with offset of the incident vortex relative to the tip of the edge ξ/θ_R. One notes good agreement between the direct force measurements $\tilde{F}_{Z-R}$ and those from integrated pressure fields $\tilde{F}_{net}$. In the latter case, pressure fluctuations downstream of $x'/\lambda = 0.5$ are not accounted

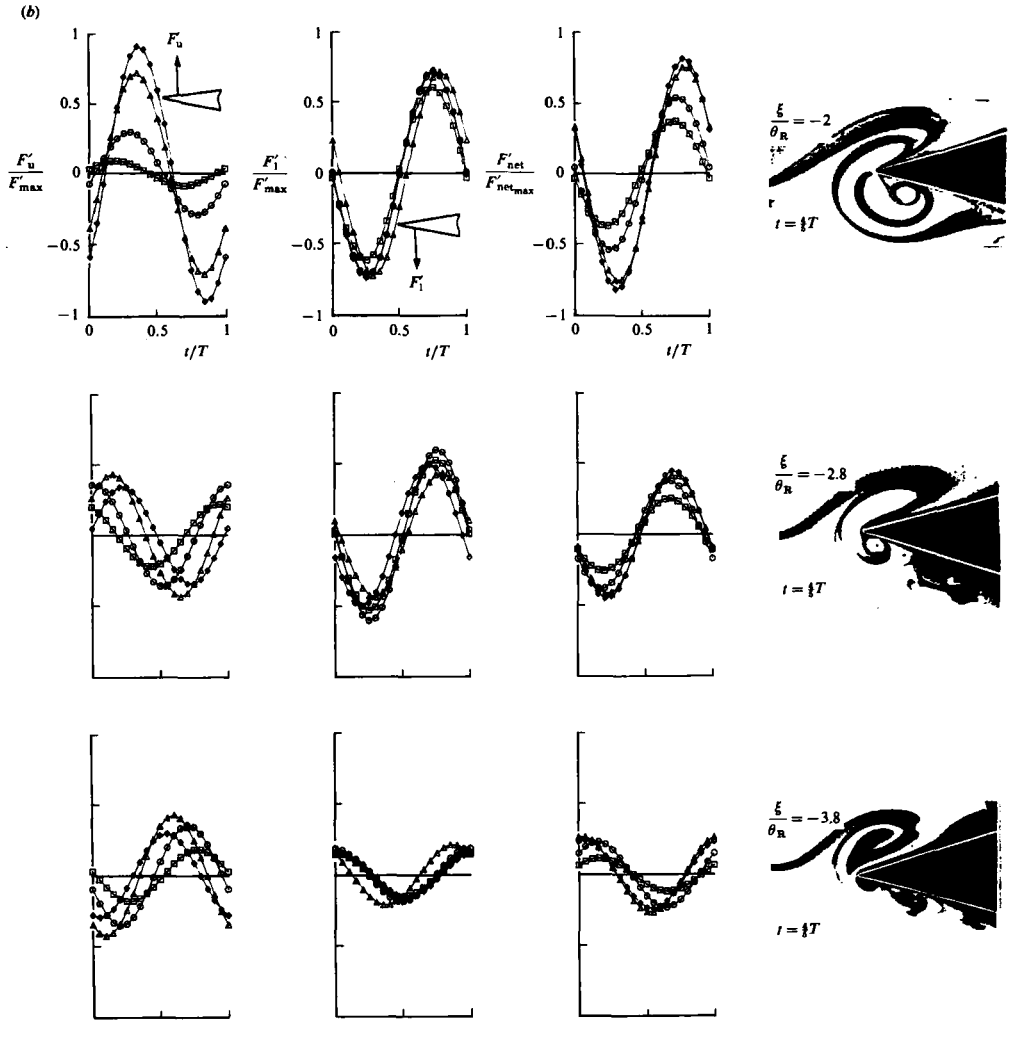

FIGURE 9. Forces on the upper (F'_u) and lower (F'_l) surfaces of edge and net force (F'_{net}) on edge over various domains of integration for varying locations of incident vortex relative to leading edge: □, $\frac{1}{12}\lambda$; ○, $\frac{1}{6}\lambda$; △, $\frac{1}{3}\lambda$; ◇, $\frac{1}{2}\lambda$.

for, and this is likely to be the primary source of discrepancy between $\tilde{F}_{Z-R}$ and $\tilde{F}_{net}$. The contributions to $\tilde{F}$ downstream of $x'/\lambda = 0.5$ are small in comparison with those at the tip of the edge. The pressure amplitude rapidly decays along the upper surface; although it remains significant on the lower surface even increasing with streamwise distance, the small wavelength provides relatively ineffective loading in this domain and a small contribution to the overall force.

Most importantly, however, we see that the relative force amplitude determined by either technique follows quite closely that of the relative leading-edge pressure, emphasizing the dominance of the tip region in determining the force on the edge.

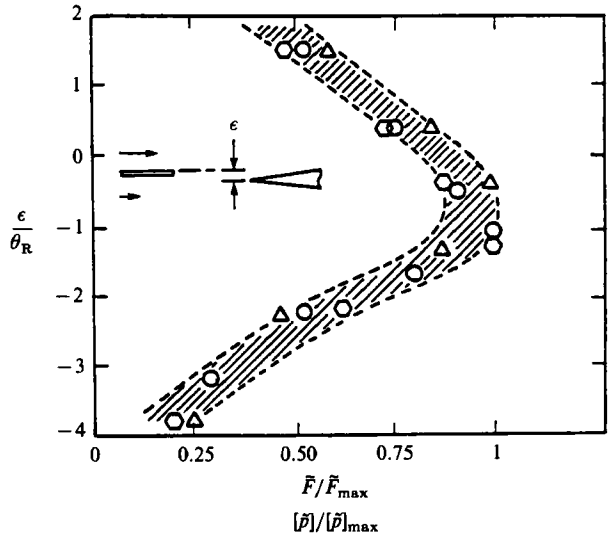

FIGURE 10. Comparison of: force at leading edge measured with strain-gauge arrangement ($\tilde{F}_{Z-R}$), ○; force determined from integrated pressure field ($\tilde{F}_{net}$), △; and leading-edge pressure $u([\tilde{p}]_{x'=0})$, ○, for various offsets of vortex with respect to leading edge.

7. Summary and conclusions

Interaction of a periodic row of vortices with an edge involves splitting of the incident vorticity field into regions passing above and below the edge. The major features of this process are: distortion/severing of the incident (primary) vortex; secondary-vortex shedding from the tip of the edge; and 'sweeping' of flow about the tip from the top to the bottom surface.

Simultaneous flow visualization and surface-pressure measurement provide the link between these mechanisms of vortex-edge interaction and the instantaneous pressure fields on the edge. Very near the tip, where rapid distortion occurs, the pressure field is non-wavelike; along the lower part of the tip, there is negligible streamwise phase variation, while the upper part of the tip shows an abrupt jump in phase. This jump is $\simeq \pi$ for cases where secondary-vortex shedding is substantial. In these cases, the pressure field takes on a wavelike character immediately downstream of the tip region; the wavelengths, and therefore phase speeds, of the pressure fields along the upper and lower surfaces of the edge differ substantially. Along the upper surface, where distortion of the incident vortex occurs, the wavelength is relatively long; along the lower surface, secondary-vortex shedding from the leading edge prevails and the wavelength is relatively short. On the average, these wavelengths along the lower and upper surfaces are substantially smaller and larger, respectively, than the wavelength of the incident row of vortices. Concerning the variation of the pressure amplitude along the surface of the edge, we see that it is maximum at the tip, due to the aforementioned 'sweeping' effect and associated secondary shedding. In fact, the tip amplitude reaches its largest magnitude when the scale of shedding is maximum. In these cases, there is rapid decay of pressure amplitude downstream of the tip.

With regard to theoretical simulation of this leading-edge pressure field, these experimental observations suggest that inviscid modelling should not incorporate a

leading-edge Kutta condition, which would require that the pressure take on a finite value as the tip is approached. Instead a singularity at the tip would seem to be most representative. In the related problem of linearized, inviscid simulation of an array of square vortices incident upon an edge, Rogler (1978) shows a singularity of order $r^{-\frac{1}{2}}$ as the tip is approached (see discussion in Z–R.) One may view the nonlinear and viscous effects manifested in secondary shedding as removing the singular behaviour at the tip.

In order to demonstrate the effectiveness of the tip region in determining the forces along the upper and lower surfaces, we have integrated the unsteady pressure field over various domains from the tip of the edge onwards. Along the lower surface, the tip region dominates owing to high pressure amplitude and the negligible streamwise phase variation there. On the other hand, the force on the upper surface is strongly dependent on the domain of integration due to the mild streamwise phase variations.

These different types of contributions to the forces on the upper and lower surfaces give, in the end, a net force amplitude that tends to be largest when the scale of the secondary-vortex shedding is most substantial, and consequently when the pressure at the tip is maximum. In fact, we are left with the remarkably simple observation: the net force along the surface of the edge scales with the magnitude of the pressure at the tip of the edge.

The authors gratefully acknowledge the primary support of the National Science Foundation, as well as supplemental support from the Office of Naval Research and the Volkswagen Foundation.

REFERENCES

CRIGHTON, D. G. 1975 Basic principles of aerodynamic noise generation. *Prog. Aero. Sci.* **16**, 31–96.

GOLDSTEIN, M. E. 1984 Aeroacoustics of turbulent shear flows. *Ann. Rev. Fluid Mech.* **16**, 263–285.

ROCKWELL, D. 1983 Oscillations of impinging shear layers. *AIAA J.* **21**, 645–664.

ROGLER, H. 1978 The interaction between vortex-array representations of free-stream turbulence and semi-infinite flat plates. *J. Fluid Mech.* **87**, 583–606.

ZIADA, S. & ROCKWELL, D. 1982 Vortex–leading-edge interaction. *J. Fluid Mech.* **118**, 79–107.

STUART, J. T. 1967 On finite amplitude oscillations in laminar mixing layers. *J. Fluid Mech.* **29**, 417–440.